MODAL ORIGIN OF THE TEMPERATURE-DEPENDENT DMA PHASE SHIFT IN POLYMER BEAMS

Leszek PYZIAK[*], Wiktoria WOJNAROWSKA[**], Michał WANIC[**], Rafał OLIWA[***], Tomasz WIĘCEK[*], Levan CHOTORLISHVILI[**]

[*]Department of Applied Optics, Faculty of Mathematics and Applied Physics, Rzeszow University of Technology, al. Powstancow Warszawy 6, Rzeszow, 35-029, Poland
[**]Department of Physics and Medical Engineering, Faculty of Mathematics and Applied Physics, Rzeszow University of Technology, al. Powstancow Warszawy 6, Rzeszow, 35-029, Poland
[***]Department of Polymer Composites, Faculty of Chemistry, Rzeszow University of Technology, al. Powstancow Warszawy 6, Rzeszow, 35-029, Poland

l.pyziak@prz.edu.pl, wwojnarowska@prz.edu.pl, mwanic@prz.edu.pl, oliwa@prz.edu.pl, ftkwiece@prz.edu.pl, l.chotorlish@prz.edu.pl

received 08 May 2026, revised 05 July 2026, accepted 14 July 2026

Abstract: Dynamic mechanical analysis is widely used to characterize viscoelastic materials, yet the physical origin of the measured phase shift remains only partially understood for structurally extended specimens. Its standard interpretation typically assumes a single, effective phase shift between applied stress and strain. In this work, we investigate the temperature-dependent viscoelastic response of medical-grade acrylonitrile butadiene styrene (ABS) fabricated by fused filament fabrication and injection molding, combining DMA measurements, fractographic analysis, and analytical modeling. Rectangular beam specimens were subjected to three-point bending DMA over a temperature range spanning the glass transition region. The storage modulus, loss modulus, and phase shift were determined as functions of temperature and compared between manufacturing routes. While both materials exhibit nearly identical glass transition temperatures, the 3D-printed samples exhibit a modest reduction in storage modulus, reflecting microstructural heterogeneity introduced by the layer-wise fabrication process. Fractographic observations reveal characteristic interlayer features and microvoids that correlate with the observed mechanical response. To interpret the temperature-dependent phase shift, we develop a theoretical model of a damped vibrating beam in which each eigenmode contributes with its own phase shift. By introducing a temperature-dependent effective damping coefficient, the model's mode-averaged phase shift reproduces the experimental DMA data with high accuracy. By linking DMA phase measurements to the mode dynamics of the tested structure, the proposed framework establishes DMA as a structure-sensitive dynamical probe and is applicable to a broad class of polymer, composite, and additively manufactured materials.

Key words: dynamic mechanical analysis, viscoelasticity, acrylonitrile butadiene styrene, fused deposition modeling, damped vibrating beam model, three-point bending, fractography

1. INTRODUCTION

Additive manufacturing (AM), commonly referred to as three-dimensional (3D) printing, has evolved into a mature fabrication technology enabling the production of geometrically complex and application-specific components, including the biomedical sector. By fabricating layer-resolved objects and using digital methods as an advanced tool, AM enables the creation of highly complex, patient-specific geometries that are difficult or impossible to produce with conventional subtractive methods. The most widely used techniques, such as fused deposition modeling (FDM), stereolithography (SLA), and selective laser sintering (SLS), allow for the processing of a diverse range of polymers, ceramics, and composites, offering versatility in both design and materials selection [1, 2, 3, 4]. Over the last decade, progress in hardware precision, bio-compatible materials, and regulatory frameworks has accelerated the adoption of 3D printing in clinical and research environments [5, 6, 7]. In medical practice, 3D printing is used to produce anatomical models, surgical guides, prosthetics, and patient-specific implants derived from imaging data, such as CT or MRI scans. Numerous studies have demonstrated its value in improving surgical accuracy, reducing operation times, and enhancing preoperative planning and medical training [8, 9, 10]. Beyond preoperative applications, an additional benefit of AM is its growing role in regenerative medicine, controlled fabrication of drug delivery systems, and tissue scaffolds [11, 12]. The integration of 3D printing into these mentioned activities supports the broader trend toward personalized and precise medicine, where treatment strategies are tailored to the anatomical and physiological requirements of individual patients [3, 13].

The success of 3D printing in medical contexts, however, relies heavily on the appropriate selection of materials that satisfy stringent biomedical standards. Polymers and composites used for biomedical applications [14, 15, 16, 17, 18], must comply with biocompatibility and purity requirements, such as those specified in ISO 10993 and U.S. Pharmacopeia Class VI. In addition to adequate mechanical and processing properties, the materials must exhibit chemical stability and the absence of cytotoxic or inflammatory components [19, 20]. As a result, significant research effort has been devoted to developing and certifying medical-grade materials engineered explicitly for contact with biological tissues. These

materials provide the foundation for the next generation of additive manufacturing in healthcare—where mechanical integrity, reproducibility, and biocompatibility converge within clinically viable designs [4, 6, 21, 22].

Common medical-grade thermoplastics include high-performance materials such as Acrylonitrile Butadiene Styrene (ABS), a thermoplastic polymer with excellent properties suitable for the healthcare industry. Namely, ABS Medical has recently gained attention as a cost-effective option for surgical guides, positioning jigs, and short-term patient-contact components [3, 23]. Compared with standard ABS, the medical-grade formulations are produced with stricter control of residual monomers and additives, and manufacturers provide certificates of analysis confirming compliance with ISO 10993-5 and USP Class VI testing. These materials are sterilizable by ethylene oxide or low temperature plasma and retain the printability and mechanical strength characteristic of ABS [11].

Although not suitable for permanent implantation, ABS Medical is widely used in short-term surgical and preoperative applications due to its mechanical robustness and documented biocompatibility. Further investigation of their mechanical behavior under additive-manufacturing conditions is therefore essential to support reliable clinical implementation [6, 24, 25]. Compared to standard ABS, ABS Medical offers a balanced combi-nation of printability, toughness, and regulatory compliance, which makes it suitable for patient-specific medical devices and surgical guides [3].

Recent studies have investigated how infill density, raster orientation, and extrusion temperature affect the tensile and flexural performance of ABS-based materials [26, 27, 28, 29]. The anisotropy inherent to fused deposition modeling (FDM) is particularly relevant for surgical tools, where directional strength and dimensional accuracy are critical. Moreover, while the certified base polymer ensures cytocompatibility, the mechanical response of the printed structure may differ from that of the bulk due to thermal gradients and residual stresses. Understanding these deviations is crucial to defining the safe design window for medical applications. Therefore, systematic evaluation of mechanical properties—tensile strength, modulus, and interlayer adhesion—under representative processing conditions is needed to establish guidelines for clinical-grade additive manufacturing with ABS Medical filaments [26, 28, 29, 30, 31, 32, 33, 34, 35].

Despite the growing body of work on the mechanical performance of additively manufactured polymers, significantly less attention has been devoted to their dynamic mechanical response, in particular to the physical interpretation of phase lag measured in dynamic loading conditions.

While our study focuses on ABS materials, our research program involves several aspects and stages. We aim to produce a comprehensive study of the problem, encompassing experimental, mechanical, and optical aspects, as well as theoretical modeling and numerical analysis. We begin our discussion by 3D printing dogbone-shaped specimens using ABS medical-grade filament. Then, using a Dynamic Mechanical Analyzer (DMA) [36], we explore the mechanical dynamical properties of the specimen. Dynamic mechanical analysis provides access to the storage modulus, loss modulus, and phase shift between applied stress and resulting strain, which are commonly interpreted within a lumped viscoelastic framework. Despite its widespread use, the physical interpretation of the phase shift measured in dynamic mechanical analysis remains largely phenomenological. In standard DMA practice, the phase lag between stress and strain is treated as a single material parameter, implicitly assuming a uniform deformation mode and neglecting the role of structural dynamics.

To gain a deeper understanding of the structure and mechanical properties, we proceed to fractographic analysis. It is well-known that the mechanical properties of a 3D-printed part are not uniform in all directions. Mechanical properties strongly depend on the direction in which the part is printed and the direction of the applied force. Using reflected-light optical microscopy, we will obtain high-resolution images of crack initiation and propagation. Our aim is to observe a correlation between fracture patterns and macroscopic mechanical behavior. This microstructural insight is essential for linking observed macroscopic mechanical response with underlying structural heterogeneity induced by the additive manufacturing process. Moreover, we construct a simple mathematical model and demonstrate that it precisely fits the measurement data. The primary experimental interest lies in the temperature-dependent phase shift observed across experiments conducted at different temperatures. Via the temperature-dependent phase shift, we extract information about the Loss modulus and Storage modulus, i.e., the two components of the complex modulus, the dynamic equivalent of Young's modulus for viscoelastic materials.

The central objective of this work is therefore to establish a physically consistent interpretation of the DMA phase shift in beam-like polymer specimens by explicitly accounting for their modal dynamics. By combining experimental measurements with theoretical modeling, we demonstrate that the phase shift should be understood as an emergent, structure-dependent quantity arising from the superposition of multiple vibrational modes.

2. EXPERIMENTAL PART

2.1. Material and methods

The experimental workflow comprised specimen fabrication, mechanical characterization, and microstructural analysis (see Fig. 1). Two fabrication methods were employed: fused filament fabrication (FDM) and injection molding, enabling a direct comparison between additively manufactured and bulk materials. This dual fabrication approach enables identification of the influence of FDM-induced structural heterogeneities, such as interlayer interfaces and porosity, on the mechanical response.

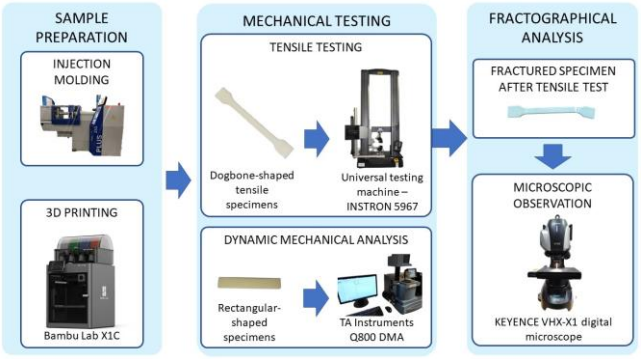

Fig. 1. Overall workflow of experimental part

ABS Medical filament was used as the model material due to its well-established mechanical properties and relevance to biomedical applications [23]. Specimens fabricated via FDM exhibited controlled geometry and internal structure, enabling experimental validation of the theoretical model. The study combines Dynamic

Mechanical Analysis (DMA), tensile testing, and fractographic inspection to characterize the mechanical response of the material under different loading conditions (Fig. 1). The complementary tensile and fractographic analyses were included to distinguish the influence of processing-induced structural heterogeneity from that of the intrinsic polymer properties when interpreting the DMA response. The experimental findings are further interpreted using a theoretical model of the observed behavior.

We note that the DMA technique allows for a comprehensive assessment of viscoelastic properties, such as storage modulus E', loss modulus E'', and the phase shift δ_{DMA}, under controlled temperature and frequency conditions, providing insight into temperature-dependent viscoelastic behavior.

$$\delta_{DMA} = \arctan\left(\frac{E''}{E'}\right) \quad (1)$$

The results of the experiments obtained via preparing the samples and producing DMA measurements, we compare with the predictions of the rigorous mathematical model discussed below.

2.1.1. Sample preparation via 3D printing

Specimens were designed using Autodesk Inventor, with two geometries tailored for dynamic mechanical analysis (DMA) and tensile testing. The geometries of the printed samples were as follows:

- DMA_sample: Rectangular bars measuring 60 mm × 10 mm × 3 mm (length × width × thickness), printed flat in the XY orientation to align the primary loading direction with the print layers and minimize interlayer effects during three-point bending DMA tests (detailed geometry shown in Fig. 2a).
- TT_sample: Dogbone-shaped tensile specimens (Type 1BA per ISO 527-2) with a total length of 150 mm, a 10 mm-wide gauge section, and enlarged gripping ends (detailed geometry shown in Fig. 2b). These were printed horizontally in the XY plane to ensure tensile loading along the filament deposition direction.

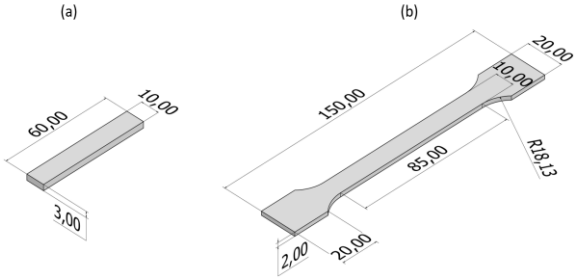

Fig. 2. Dimensions of the samples used in the experiments: (a) samples used for DMA, (b) samples used for mechanical testing

The samples were prepared via FDM using a Bambu Lab X1C 3D printer equipped with a 0.4 mm hardened steel nozzle. A medical-grade ABS filament (ABS Medical, 1.75 mm diameter, natural color, Spectrum Filaments) was used, selected for its well-defined properties and suitability for 3D printing. Both sample types were processed under identical optimized parameters to achieve dense, void-free specimens with consistent layer bonding and minimal anisotropy.

Before printing, the filaments were dried at 80°C for 4 hours in a forced-air laboratory oven to remove any moisture absorbed on the surface. Key printing settings are summarized in Table 1.

Tab. 1. Parameters of printed samples

Parameter	Value
Nozzle temperature	255 °C
Bed temperature	100 °C
Infill density	100%
Infill pattern	Rectilinear
Printing speed	100 mm/s
Nozzle size	0.4 mm
Nozzle type	stainless steel
Layer height	0.20 mm
Layer width	0.42 mm
Active cooling fan	15%
Shell	2
Chamber environment	enclosed, passively heated

A total of 10 DMA_samples and 10 TT_samples were produced in a single build to minimize batch-to-batch variability. All printing and post-processing were conducted in a controlled laboratory environment maintained at 23 ± 1°C and 50 ± 3% relative humidity. Following printing, samples were removed from the build plate after a 30-minute cooldown period to prevent thermal distortion. Each specimen was visually inspected and measured using a digital caliper (accuracy ±0.01 mm) to confirm dimensional compliance.

2.1.2. Sample preparation via injection molding

Injection-molded specimens were used as reference material. The samples were manufactured using a Battenfeld 350 PLUS injection molding machine (WITTMANN BATTENFELD GmbH, Germany) with a screw diameter of $D = 25\ mm$ and a length-to-diameter ratio (L/D) of 17. The processing parameters were as follows: heating zone temperatures of $245°C$, $250°C$, and $250°C$, mold temperature of 60°C, injection pressure of 425 bar, holding pressure of 425 bar, holding time of 5 s, and cooling time of 15 s.

2.1.3. DMA measurements

The viscoelastic properties of the DMA_sample specimens were characterized using a TA Instruments Q800 dynamic mechanical analyzer operating in three-point bending mode (Fig. 3). The test configuration consisted of a support span $L = 50\ mm$.

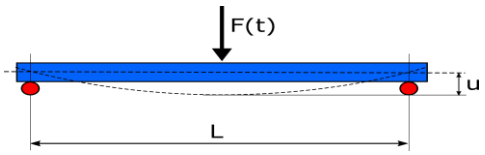

Fig. 3. Schematic representation of the DMA three-point bending configuration, where L – support span (50 mm); F – applied oscillatory force; u – mid-span vertical displacement (oscillatory deflection)

Rectangular DMA_sample specimens (geometry defined in section 2.1.1 and shown in Fig. 2a) were tested in accordance with ASTM D4065. The specimen width (b) and thickness (h) were measured individually prior to testing and used for modulus calculations.

Prior to measurement, specimens were equilibrated at 25°C for 5 min. A temperature sweep was conducted from 25°C to 140°C at a constant heating rate of 3°C min−1. Oscillatory deformation was

applied at a fixed frequency of 1 Hz with a displacement amplitude of 15 μm.

The heating rate and excitation frequency were adopted in accordance with established DMA protocols for thermoplastic polymers and FDM-printed ABS-based materials reported in the literature, where similar conditions (2–5 °C/min and 1–3 Hz) are commonly used under ASTM D4065-compliant setups [28, 37]. These conditions ensure a balance between thermal equilibration and measurement resolution, reducing thermal lag effects while preserving reliable detection of the glass transition. The selected amplitude was verified to be within the linear viscoelastic region by a preliminary amplitude sweep performed at 23°C.

While the present study is limited to a single excitation frequency (1 Hz), this choice ensures direct comparability with standard DMA bending-mode protocols and isolates temperature-dependent effects relevant to the proposed model. A systematic frequency sweep and its influence on model parameters are identified as future work to further evaluate the frequency dependence of the proposed theoretical framework.

Key output parameters, such as storage modulus (E'), loss modulus (E''), and damping factor ($\tan\delta = E'' / E'$) were recorded as functions of temperature. The glass transition temperature (T_g) was determined from the peak of the tan δ curve, with additional confirmation from the onset of the storage modulus decrease and the peak of the loss modulus curve. A minimum of $n = 10$ specimens were tested to ensure statistical reliability. All measurements were conducted under controlled laboratory air atmosphere.

2.1.4. Tensile testing

Tensile strength was studied according to ISO 527-1:1998 standard using Instron 5967 testing machine. Elongation speed was $0{,}5\ \mathrm{mm/min}$ for the elastic region after that the tension speed was increased to $5\ \mathrm{mm/min}$. Samples in the form of paddles were used (TT_sample). Based on the tension test the tensile yield strength, Young's modulus, strain at yield stress and strain at break were determined. The results are presented as arithmetic means from five tests for both injection-molded and 3D-printed sample.

2.1.5. Fractographic analysis

One representative specimen that had fractured during mechanical testing was selected for fractographic analysis. Its fracture surface was examined using a KEYENCE VHX-X1 digital microscope in reflected light mode. Images were acquired at magnifications of 20×, 100×, and 200× without applying any conductive coating. High-resolution imaging allowed documentation of the fracture surface, including crack initiation and propagation features, layer interfaces, and filament deposition paths in the FDM-printed ABS Medical specimen. The analysis was primarily qualitative, enabling visual assessment of characteristic defects and the microstructural architecture of the printed material.

2.2. Results of the experimental part

2.2.1. Mechanical properties

As a terpolymer, ABS consists of varying proportions of acrylonitrile, butadiene, and styrene. Due to the different chemical structures and compositions of the individual monomers, they are responsible for the different properties of ABS. Acrylonitrile improves the chemical resistance and thermal stability. Butadiene, provides the material with flexibility and impact resistance, whereas styrene, is responsible for the dimensional stability and rigidity of the material. As a result, in terms of mechanical properties and sample response to sinusoidally varying stress in DMA analysis, two phases of ABS can be distinguished: the rigid phase, which is formed by styrene-acrylonitrile segments responsible for, among other things, glass transition temperature and modulus, and the butadiene phase responsible for impact strength and vibration damping. Based on the measurements, the relationships between E', E'' and $\tan\delta$ as a function of temperature and glass transition temperature were obtained (Fig. 4), which were described and compared between the tested ABS samples – obtained by injection molding and 3D printing. The obtained glass transition temperatures of printed and injection-molded samples are within the range of literature data and, notably, are very similar to each other, with a difference of ±0.5°C [28, 37]. According to the literature data, the storage modulus decreases with temperature, and when the temperature reaches approx. 103°C, it drops sharply, indicating an increase in the mobility of ABS rigid segments and a loss of material elasticity, regardless of the material [38]. However, a lower E' value was observed for printed ABS, which may indicate a more heterogeneous structure caused by the presence of voids, anisotropy, layered structure, and sliding at the layer-to-layer interface. The differences recorded are minor, E'' and $\tan\delta$ which also resulted in similar glass transition temperatures for max E'' and $\tan\delta$, which are approx. 1°C lower for the printed material. A similar trend was observed for the E'' modulus, especially in the glass transition region. Greater energy storage capacity (E') resulted in the ability to dissipate a greater absolute amount of energy in solid materials. However, the ability to suppress energy is the same, as indicated by the overlap of the $\tan\delta$ curves. Therefore, it can be concluded that both samples are chemically and molecularly equivalent, and the same SAN exhibits a glass transition. In turn, the influence of printing-induced microstructure on the glass transition temperature is negligible, while structural dynamics govern the measured phase shift.

The results of tensile testing, expressed as arithmetic means from five measurements for injection-moulded and 3D-printed ABS samples, are summarized in Table 2. Representative tensile stress–strain curves are shown in Figure 5. Statistical significance of the differences between the two manufacturing methods was assessed using Welch's t-test, and the corresponding p-values are reported in Table 2. The obtained results indicate statistically significant differences in all evaluated mechanical properties ($p < 0.001$).

The presented curves indicate a non-linear tensile behavior of the printed and injection-molded samples and are characteristic of elastic-plastic materials, in accordance with the literature data [24, 26, 39]. Both ABS_IM and ABS_3D exhibit elastic deformation limits and yield points. Nevertheless, the changes are more pronounced for injection-molded sample. After the yield point is reached, there is a sharp decrease in stress and a plateau in the stress-strain relationship. Whereas for a ABS_3D sample, after the maximum tensile stress is reached, there is a slight continuous decrease in its value up to the moment of sample breakage. This behavior is directly related to the heterogeneous and layered structure of the printed sample, as revealed during the morphological analysis. The presence of interlayer interfaces and internal voids reduces the effective load-bearing cross-sectional area, promoting earlier

stress localization and premature failure. Due to its heterogeneous structure, the sample is more flexible, as evidenced by its lower Young's modulus, which also confirms the results obtained during DMA analysis.

As a result, the nature of the fracture is more ductile. Whereas for the injection-molded sample, after reaching a clear plateau, a slight increase in tensile stress is observed, reflecting minor strain hardening due to polymer chain orientation. The final phase behavior is similar to brittle fracture, although the overall sample still undergoes significant plastic deformation.

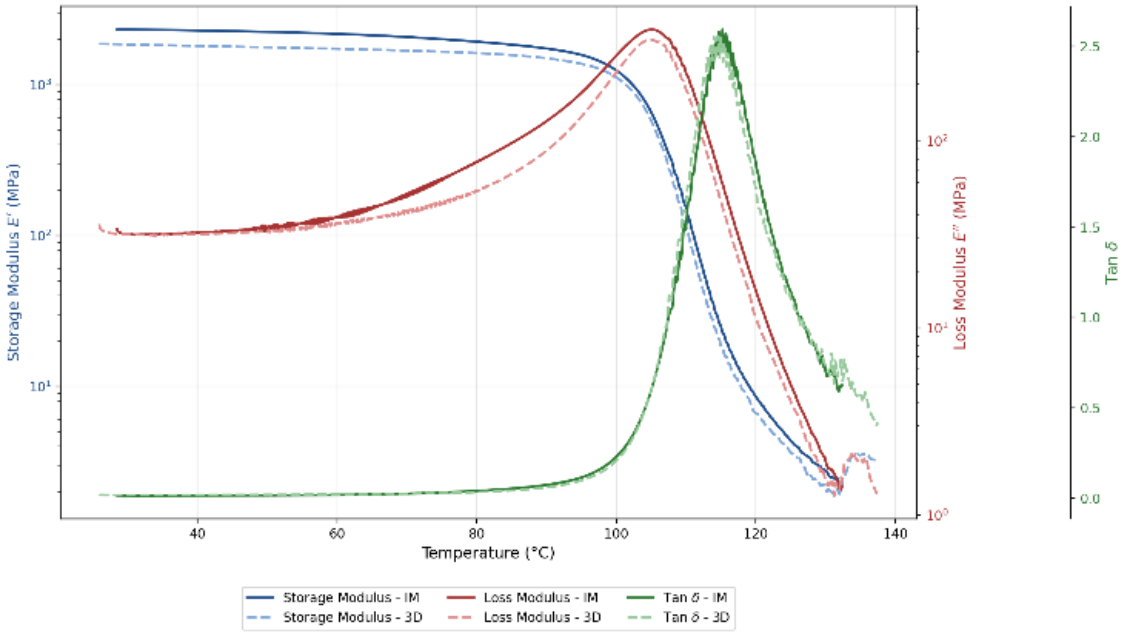

Fig. 4. Storage modulus (E', black lines), loss modulus (E", blue lines), and $\tan\delta$ (red lines) obtained by DMA measurements for a sample from injection molding (solid lines) and 3D printing (dashed lines)

Tab. 2. Mechanical properties of ABS sample

Sample symbol	Injection_ ABS	3D_ABS	p-value
Tensile yield strength [MPa]	42.2±1.9	29.6±3.4	<0.001
Young modulus [MPa]	1820.7±14.9	1328.4±21.5	<0.001
Strain at tensile yield [%]	2.8±0.1	2.2±0.1	<0.001
Strain at break [%]	37.3±6.2	9.2±2.0	<0.001

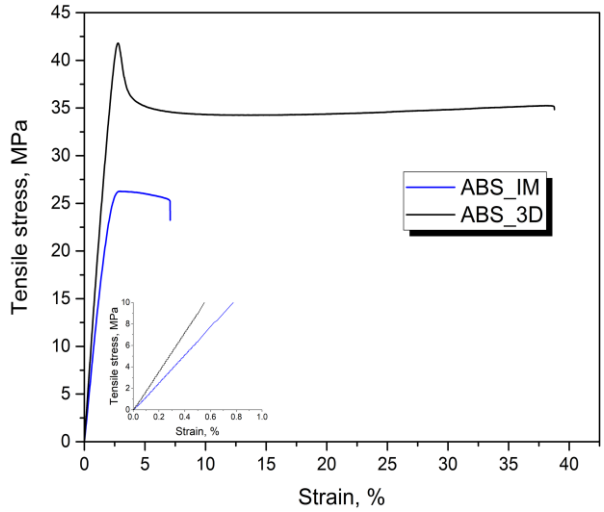

Fig. 5. Tensile stress vs. Strain of ABS sample made using 3D printing (ABS_3D) and injection molding (ABS_IM)

The presented curves indicate a non-linear tensile behavior of the printed and injection-molded samples and are characteristic of elastic-plastic materials, in accordance with the literature data [24, 26, 39]. Both ABS_IM and ABS_3D exhibit elastic deformation limits and yield points. Nevertheless, the changes are more pronounced for injection-molded sample. After the yield point is reached, there is a sharp decrease in stress and a plateau in the stress-strain relationship. Whereas for a ABS_3D sample, after the maximum tensile stress is reached, there is a slight continuous decrease in its value up to the moment of sample breakage. This behavior is directly related to the heterogeneous and layered structure of the printed sample, as revealed during the morphological analysis. The presence of interlayer interfaces and internal voids reduces the effective load-bearing cross-sectional area, promoting earlier stress localization and premature failure. Due to its heterogeneous structure, the sample is more flexible, as evidenced by its lower Young's modulus, which also confirms the results obtained during DMA analysis. As a result, the nature of the fracture is more ductile. Whereas for the injection-molded sample, after reaching a clear plateau, a slight increase in tensile stress is observed, reflecting minor strain hardening due to polymer chain orientation. The final phase behavior is similar to brittle fracture, although the overall sample still undergoes significant plastic deformation.

2.2.2. Morphology of fracture surfaces of a polymer sample

We observed a clear correlation between fracture patterns and macroscopic mechanical behavior for both FDM printed and injection-molded ABS samples. The crack location and propagation on

the side surface are shown for the FDM-printed sample in Figure 6a and for the injection-molded sample in Figure 6c, with cross-sectional views in Figures 6b and d, respectively.

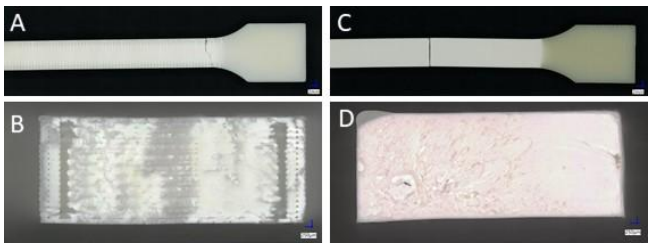

Fig. 6. Fracture characterization of ABS medical filament: (a) FDM-printed sample – side view at 20× magnification, indicating crack location; (b) FDM-printed sample – cross-sectional view at 100× magnification, showing crack propagation and material morphology; (c) Injection-molded sample – side view at 20× magnification, indicating crack location; (d) Injection-molded sample – cross-sectional view at 100× magnification, showing crack propagation and material morphology

In four out of five FDM-printed specimens, crack initiation occurred at the geometric transition between the narrow section of the sample and the grip region, corresponding to the location shown in Figure 6a. However, in one specimen, the cracking occurred in the middle of the narrow section. Crack propagation was irregular, exhibiting characteristic deflections aligned with the 3D printing paths, which were oriented at approximately 45° to the tensile axis. This orientation-dependent fracture behavior reflects the anisotropic nature of FDM-printed materials and is consistent with previous findings demonstrating that raster angle and interlayer bonding significantly affect tensile performance and crack development in ABS structures [40, 41].

In contrast, the injection-molded specimen showed a more linear and symmetric crack path, initiating primarily at regions of local stress concentration, without evidence of directionally biased deflection (Fig. 6c).

The overall fracture surface of the FDM-printed samples (Fig. 6b) reveals regular semicircular outlines corresponding to individual filament deposition paths characteristic of FDM technology, while the overall fracture surface exhibits a heterogeneous structure with clearly defined layer boundaries. In the central region, areas with heterogeneous texture and variable tonal contrast indicate differences in cohesion between adjacent paths. This structure suggests the presence of local microvoids and incomplete fusion, which may reduce load-bearing capacity in directions perpendicular to the extrusion axis.

Higher-magnification fractographic features show peripheral layer morphology, microvoids, and zones of stable and final crack propagation (Figure 7a–c). The stable propagation region is characterized by relatively smooth topography and subtle beach marks, whereas the final fracture zone exhibits rough, fibrous morphology indicative of ductile failure. The fracture behaviour of the FDM-printed ABS medical filament observed in this study is consistent with the general mechanisms reported in the literature for ABS materials. As described by Lach et al. (2001) [42], fracture surfaces can be divided into zones of stable and unstable crack growth, with smooth regions corresponding to gradual propagation and rough, fibrous areas reflecting final overload. In the present printed samples, however, these classical zones are strongly influenced by the layered FDM structure, including semicircular filament perimeters, inter-layer voids, and local delamination, which serve as primary sites for crack initiation and anisotropic propagation. These observations are further supported by Boğa (2021) [41], who demonstrated that fracture paths and surface morphology in 3D-printed ABS strongly depend on deposition pattern, layer orientation, and local microstructural heterogeneities.

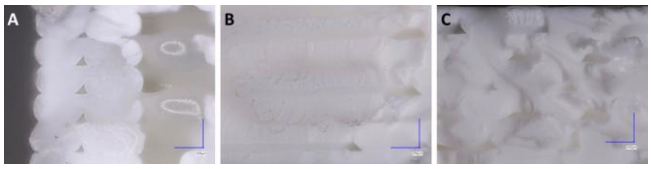

Fig. 7. Microphotographs of fracture surface of FDM-printed sample at 200× magnification: (a) Peripheral and layer morphology showing semicircular perimeters, triangular layer imprints, and microvoids indicative of potential crack initiation sites; (b) Stable crack propagation region with smooth topography and gentle beach marks along inter-layer boundaries; (c) Final overload fracture region, exhibiting chaotic, fibrous structures and crushed filament paths, indicative of ductile rupture beyond the material's ultimate strength

To complement the qualitative fractographic observations, a preliminary quantitative image analysis was performed using ImageJ on the triangular inter-raster voids visible in the peripheral layer region (Fig. 7a). A representative region of interest was extracted and processed by threshold-based segmentation, as illustrated in Fig. 8a–b. Within this region, six measurable inter-raster voids were identified, exhibiting a mean area of 1761.5± 611.3 $\mu m2$ (range: 765–2300 $\mu m2$; Table 3). These voids originate from the geometric packing of adjacent filament rasters during the FDM deposition process and therefore represent process-inherent porosity rather than damage-induced microvoids formed during tensile loading. The presence of such process-inherent voids is qualitatively consistent with the significantly lower tensile yield strength, Young's modulus, and strain at break observed for the FDM-printed specimens compared with the injection-moulded counterparts (Table 2, all $p < 0.001$), suggesting that they may promote local stress concentration and facilitate crack initiation. Since the quantitative analysis was limited to a single representative field of view, these observations should be regarded as preliminary and indicative rather than statistically representative.

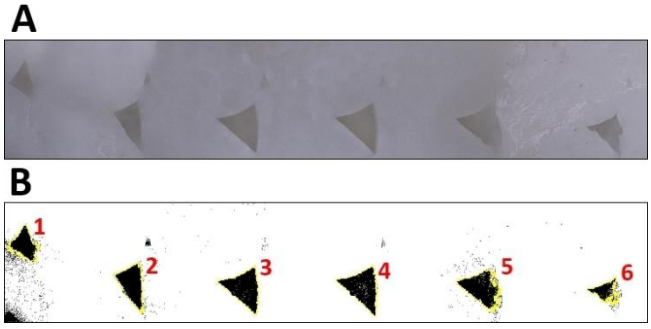

Fig. 8. Quantitative segmentation of triangular inter-raster voids in the FDM-printed sample: (a) cropped region of interest from Fig. 7a prior to segmentation; (b) corresponding binary mask after threshold-based segmentation in ImageJ, with detected voids outlined

Tab. 3. Quantitative analysis of triangular inter-raster voids identified via ImageJ segmentation (single representative field of view, FDM-printed sample)

Void No.	Area (μm^2)
1	1316
2	1803
3	2275
4	2300
5	2110
6	765
Mean ± SD	1761.5±611.3

Injection-molded samples, in contrast, exhibit smoother, more homogeneous surfaces (Fig. 6d and Fig. 9a-c), with uniformly distributed microvoids characteristic of ductile ABS fracture. Stable crack propagation regions display isotropic morphology, while the final overload zones show fibrous features. The higher structural uniformity observed in injection-molded specimens is consistent with previously reported improvements in mechanical performance of injection-molded ABS compared to FDM-printed counterparts [40]. Czyżewski et al. (2024) [43] further emphasized that injection molding promotes higher density and improved interfacial cohesion, which directly translate into greater Young's modulus and strength compared to additively manufactured counterparts.

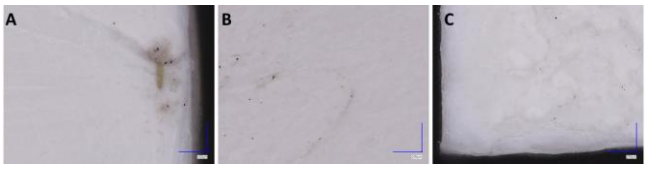

Fig. 9. Microphotographs of fracture surface of injection-molded ABS sample at 200× magnification: (a) Crack initiation region with relatively smooth morphology; (b) Stable crack propagation region showing a semicircular depression and local propagation markings indicative of crack front progression; (c) Final overload region characterized by rough, irregular surface morphology and evidence of ductile tearing

The similarity in glass transition temperature suggests that the observed differences in mechanical performance are primarily associated with processing-induced microstructural heterogeneity rather than chemical or molecular variations between the samples. Overall, the fracture behavior of FDM-printed ABS is governed by layer morphology, interfacial cohesion, internal porosity, and printing-induced anisotropy, whereas injection-molded ABS exhibits fracture characteristics dominated by isotropic material properties and inherent structural uniformity. The present observations therefore align with classical ABS fracture theory [42] and with modern comparative studies highlighting the decisive role of processing-induced microstructure in determining crack initiation and propagation mechanisms [40, 41, 43].

$$G(x,\xi,t) = \frac{2L}{a\pi^2}\sum_{n=1}^{\infty}\frac{\Omega_n e^{-\gamma t}}{n^2\beta_n}\sin(\eta_n x)\sin(\eta_n \xi)\sin(\beta_n t) \quad (6)$$

3. THEORETICAL MODEL

$$u(x,t) = \frac{4LF_0}{ma\pi^2}\sum_{n=0}^{\infty}\frac{\sin(\eta_{2n+1}x)}{(2n+1)^2}f_{2n+1,\gamma}(t) \quad (7)$$

In conventional DMA analysis, the specimen is treated as a lumped viscoelastic element, and the measured phase shift is directly associated with the ratio of loss and storage moduli. However, for beam-like specimens, the deformation field is inherently non-uniform and can be decomposed into a hierarchy of vibrational eigenmodes. Each mode responds to harmonic excitation with its own phase shift, governed by its natural frequency and damping. The model reveals a fundamental limitation of the standard DMA formalism when applied to extended structures: the experimentally measured phase shift does not correspond to a single material parameter, but to a weighted average over structurally defined dynamical modes.

Here we show that the DMA phase shift of beam-like polymer specimens cannot, in general, be attributed to a single relaxation process. Instead, it emerges as a collective response of multiple vibrational eigenmodes, each characterized by its own phase shift and participation weight. Namely, we prove that each oscillation mode has its own phase shift. While the participation rates of the different modes differ, their contribution decreases with increasing mode number. Nevertheless, the phase shift averaged over the modes fits well with the experimental results. For the theoretical modeling of the process, we exploit a partial differential equation, the Euler–Lagrange equation derived for the following action:

$$S = \int_{t_1}^{t_2}\int_0^L \mathcal{L}[\,t,\,u(x,t),\partial_{xx}u(x,t),\,\partial_t u(x,t)]\;dxdt$$

$$\frac{\partial}{\partial t}\left(\frac{\partial \mathcal{L}}{\partial u_t(x,t)}\right) = \frac{\partial^2}{\partial x^2}\left(\frac{\partial \mathcal{L}}{\partial u_{xx}(x,t)}\right) + \frac{\partial \mathcal{L}}{\partial u(x,t)} - \frac{\partial D}{\partial u_t(x,t)} \quad (2)$$

Here $\mathcal{L}[t,u(x,t),\partial_t u(x,t)]$ is the Lagrange function

$$\mathcal{L}[t,u(x,t),\partial_t u(x,t)] == \frac{1}{2}m\left(\frac{\partial u(x,t)}{\partial t}\right)^2 - \frac{1}{2}EJ\left(\frac{\partial^2 u(x,t)}{\partial x^2}\right)^2 + Fu(x,t) \quad (3)$$

where

$a^2 = EJ/(\rho A)$, E is the Young's modulus of the material, A is the cross-sectional area of the beam, $J = bh^3/12$ the second moment of area of the beam cross-section, the beam length l, breadth b,and thickness h. The external driving term we choose in the form $F(t) = F_0\sin(\omega t)$ with driving amplitude F_0 and frequency ω, m is the mass of the beam per unit length, and the dissipation function reads $D = m\gamma\left(\frac{\partial u}{\partial t}\right)^2$. In the case of a uniform beam, the equation takes a $D = m\gamma\,\partial t$ simpler form [44]:

$$\frac{\partial^2 u(x,t)}{\partial t^2} + a^2\frac{\partial^4 u(x,t)}{\partial x^4} + 2\gamma\frac{\partial u(x,t)}{\partial t} = \frac{1}{m}F(x,t) \quad (4)$$

In what follows, the temperature-dependent effective damping constant $\gamma(T)$ is a free parameter of the theory that we tune to fit the experimental data. To solve Eq.(4) we adopt the supported boundary conditions $u(0,t) = u(L,t) = 0$, and $\partial_{xx}u(x,t) = 0$ for $x = 0, L$. The general solution of Eq.(4) can be presented in the form:

$$u(x,t) = \left(2\gamma + \frac{\partial}{\partial t}\right)\int_0^L u(\xi,0)G(x,\xi,t)d\xi + \int_0^L \partial_t u(\xi,0)G(x,\xi,t)d\xi + \frac{F_0}{m}\int_0^t\int_0^L G(x,\xi,t-\tau)\sin(\omega\tau)\,d\xi d\tau \quad (5)$$

The explicit form of the Green function depends on the boundary conditions. For the supported boundary conditions where $\eta_n = n\pi/L$. Taking into account Eq.(5), Eq.(6) we present the solution in the form

$$u(x,t) = \frac{4LF_0}{ma\pi^2}\sum_{n=0}^{\infty}\frac{\sin(\eta_{2n+1}x)}{(2n+1)^2}f_{2n+1,\gamma}(t) \quad (7)$$

Here

$$f_{n,\gamma}(t) = \frac{\Omega_n}{\eta_n D_n}\Big[(\Omega_n^2 - \omega^2)\sin(\omega t) - 2\gamma\omega\cos(\omega t) + e^{-\gamma t}\left(2\gamma\omega\cos(\beta_n t) + \frac{\omega(\omega^2+2\gamma^2-\Omega_n^2)}{\beta_n}\sin(\beta_n t)\right)\Big] \quad (8)$$

with the following introduced notation: $\gamma \equiv \gamma(T)$ is the damping constant, $D_n = (\Omega_n^2 - \omega^2)^2 + 4\gamma^2\omega^2$.

Taking into account Eqs. (7), (8) we present the solution in the form

$$u(x,t) = \sum_{n=0}^{\infty} u_{2n+1}(x,t,\delta_{2n+1}) \quad (9)$$

$$u_{2n+1}(x,t,\delta_{2n+1}) = \frac{4LF_0}{ma\pi^2}\frac{\sin(\eta_{2n+1}x)}{(2n+1)^2} f_{2n+1,\gamma}(t) \quad (10)$$

Here δ_{2n+1} is the phase shift of the $2n+1$th mode defined by

$$\tan(\delta_{2n+1}) = \frac{2\gamma\omega}{\Omega_{2n+1}^2 - \omega^2} \quad (11)$$

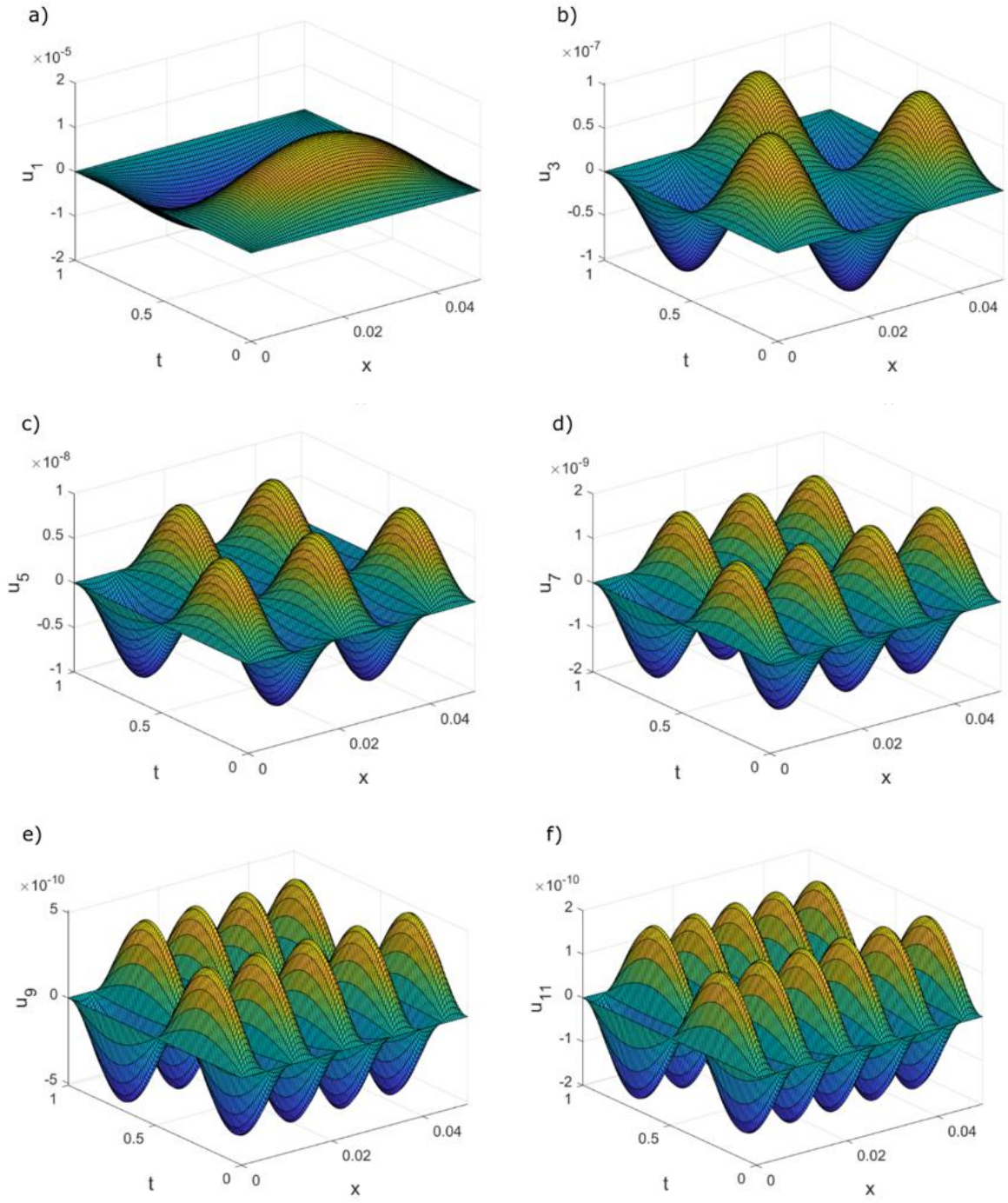

Fig. 10. Three-dimensional plots of the beam deflection $u_n(x,t)$ for a vibrating beam of length L in successive eigenmodes: (a) $n = 1$, (b) $n = 3$, (c) $n = 5$, (d) $n = 7$, (e) $n = 9$, (f) $n = 11$. Axes: position x along the beam ($0 \le x \le L$), time t over one full period of the corresponding mode ($0 \le t \le T$), and transverse deflection $u_n(x,t)$. Each subplot illustrates the temporal evolution of the beam shape for the respective mode

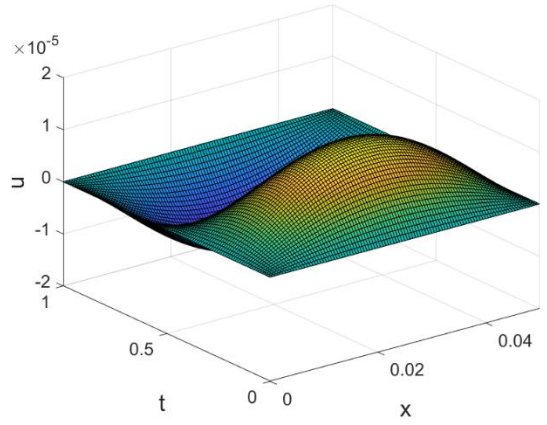

Fig. 11. Three-dimensional plot of the total beam deflection $u(x,t) = \sum_{n=0}^{5} u_{2n+1}(x,t)$, obtained by superposing all six eigenmodes shown in Fig. 10. Axes: position x along the beam $0 \le x \le L$, time t over one full period of the fundamental mode $0 \le t \le T$, and transverse deflection $u(x,t)$. The plot illustrates the complex temporal evolution of the beam shape resulting from the linear combination of the first six modes.

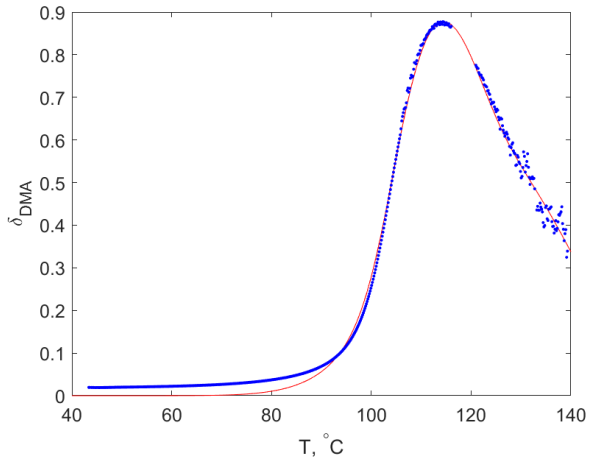

Fig. 12. Temperature dependence of δ_{DMA}, where blue dots represent experimental data fitted by the Gaussian function and the red line is obtained via the solution of Eq.(7).

We considered the supported boundary conditions because it precisely matches our DMA setup and experiment. On the other hand, our theoretical approach is not limited for particular boundary conditions. different alternative boundary conditions can be implemented depending on the experimental interest. We note that the amplitudes of individual $u_n(x,t)$ decrease with increasing mode number n. Due to the symmetric loading, only odd modes are excited (see Eq. (9)). Therefore, the solution of the partial differential equation (9) qualitatively follows the first mode $u(x,t) \approx u_1(x,t)$, while the contribution of the third mode $u_3(x,t)$ is on the order of 1%, (see Fig.10 and Fig. 11).

In the experiment, the phase shift is measured in the middle of the beam $x = L/2$, at a particular moment of time $t = t_m$. Therefore, the averaged phase shift governed by Eqs. (9)-(11) reads:

$$\langle\delta\rangle = \sum_{n=0}^{\infty} P_{2n+1} \arctan\left(\frac{2\gamma(T)\omega}{\Omega_{2n+1}^2 - \omega^2}\right) \tag{12}$$

where

$$\mathcal{P}_{2n+1} = \frac{u_{2n+1}(L/2,t_m)}{\sum_n^{\infty} u_{2n+1}(L/2,t_m)} \tag{13}$$

quantifies the participation rate of the nth mode. The total dissipated energy during the one period of oscillation $T = 2\pi/\omega$ reads:

$$E_d = \sum_{n=0}^{\infty} \frac{16\pi\omega F_0^2 \gamma(T)}{mL\eta_{2n+1}^2\left[\left(\Omega_{2n+1}^2 - \omega^2\right)^2 + 4\gamma^2(T)\omega^2\right]} \tag{14}$$

In the experiment, DMA evaluates the phase shift using the simpler arguments: Considering the driving force:

$$F^{DMA}(t) = F_0^{DMA} \sin(\omega t) \tag{15}$$

and response

$$u^{DMA}(t) = u_0^{DMA} \sin(\omega t - \delta_{DMA}) \tag{16}$$

DMA calculates the phase shift δ_{DMA} via the time delay between peaks of driving stress $F^{DMA}(t)$ and strain:$u^{DMA}(t)$

$$\delta_{DMA} = \omega \Delta t \tag{17}$$

which can be also defined as equation (1). To compare experimental and theoretical results, we numerically solve the equation:

$$\delta_{DMA} = \langle\delta\rangle \tag{18}$$

and fit temperature dependence of damping constant $\gamma(T)$.

The results of the experimental measurements and theoretical modeling presented in Fig.12 confirm the quantitative.

4. DISCUSSION

4.1. Structure-dependent interpretation of DMA phase shift

The present results indicate that the phase shift measured in dynamic mechanical analysis of beam-like specimens should be interpreted as an emergent, structure-dependent quantity rather than as a direct proxy for a single intrinsic material relaxation process. While conventional DMA implicitly assumes uniform deformation and a lumped-viscoelastic response, extended specimens subjected to bending necessarily exhibit non-uniform displacement fields that can be decomposed into a hierarchy of vibrational eigenmodes. Each of these modes responds to harmonic excitation with a characteristic phase shift determined by its natural frequency and damping, and the experimentally observed phase lag reflects a weighted superposition of their contributions. The theoretical model developed in this work quantitatively supports this interpretation, demonstrating that the measured phase shift can be accurately reproduced by considering modal superposition with a temperature-dependent damping coefficient. From this perspective, the temperature dependence of the DMA phase shift encodes not only changes in intrinsic viscoelastic dissipation but also the modal structure of the tested geometry.

Although medical-grade ABS was employed here as a representative polymer system with well-defined processing routes, the proposed framework is applicable to a broad class of polymeric and composite materials, particularly those produced by additive manufacturing or possessing internal architectural heterogeneity. This

is especially relevant for FDM-fabricated structures, where anisotropy, interlayer bonding, and internal porosity modify both stiffness and damping characteristics, thereby influencing modal participation and the resulting phase response. The results, therefore, suggest that DMA, when applied to structured specimens, can be viewed as a structure-sensitive dynamical probe, and that caution is required when interpreting phase-shift data solely in terms of material rheology without accounting for structural dynamics. From a practical standpoint, this implies that comparisons of DMA data across different specimen geometries or fabrication routes should be performed with care, as differences in phase shift may reflect not only material properties but also structural and modal effects.

4.2. Applicability to other boundary conditions and loading configurations

The experimental validation presented in this work is limited to the simply supported beam under three-point bending because this configuration corresponds to the capabilities of the employed DMA setup and represents a standard testing configuration in dynamic mechanical analysis [36]. Nevertheless, the proposed modal superposition framework is not inherently restricted to this particular boundary condition. The proposed framework is based on the decomposition of the structural response into vibration eigenmodes, and its extension to other beam configurations, such as cantilever or clamped-clamped systems, primarily requires incorporation of the corresponding mode shapes and natural frequencies into the modal expansion. As discussed by Yamada et al. [45], modal formulations can be generalized to a broad range of boundary conditions, although increasingly complex support conditions may require dedicated analytical treatments or numerical determination of the eigenmodes.

Extension to loading configurations other than three-point bending would require reformulation of the corresponding displacement fields and modal participation while preserving the underlying modal superposition principle. Experimental verification of such configurations is beyond the scope of the present study because the available DMA instrumentation is limited to standard three-point bending tests. Future experimental validation involving alternative boundary conditions and loading configurations will be important for assessing the generality and predictive capability of the proposed framework.

4.3. Methodological outlook

This study is based on a traditional analytical modal superposition framework, which provides a mechanistically transparent description of the observed dynamic mechanical response. However, its applicability becomes limited for complex geometries, nonlinear material behavior, multiphysics coupling, and process parameter optimization. Future work could therefore combine the present physics-based formulation with data-driven and physics-informed approaches to enhance model generalizability while preserving physical interpretability.

Conceptually, the proposed modal formulation could serve as a physics-based prior within a hybrid machinelearning framework. Instead of predicting DMA responses solely from data, neural networks could be trained to identify unknown temperature-dependent material parameters or modal participation factors while maintaining the modal superposition constraints derived from the present model. Such an approach would extend the applicability of the model to complex geometries and heterogeneous polymer systems where explicit analytical solutions become impractical.

In particular, the CF-DeepONet framework proposed by Zheng et al. [46] demonstrates the capability of deep operator networks to learn nonlinear mappings between functional inputs and output fields using a trunk–branch architecture. In the context of DMA analysis, a similar operator-learning strategy could approximate the relationship between temperature evolution, excitation frequency, specimen geometry, and the corresponding storage modulus and phase shift, while being constrained by the analytical modal formulation developed in the present work.

Similarly, the T-phPINN framework proposed by Zheng et al. [47] illustrates how physics-informed neural networks incorporate governing physical relationships into the learning process to improve predictions of complex thermophysical fields. This approach is particularly relevant for thermomechanically coupled DMA, where heat generation from viscoelastic dissipation may introduce local temperature gradients affecting the measured phase response. In the present framework, the analytical modal formulation could serve as a physics-based prior during network training, enabling the inference of unknown temperature-dependent material parameters from experimental DMA data while preserving physical interpretability and extending applicability to complex geometries and heterogeneous polymer systems where explicit analytical solutions become impractical.

Finally, surrogate-based optimization frameworks combining PINNs, deep active learning, and reinforcement learning provide efficient strategies for exploring high dimensional design spaces [48]. In future work, these methods may be applied to optimize both processing and testing parameters in additively manufactured polymers, including layer height, printing orientation, annealing conditions, as well as DMA testing conditions such as frequency and heating rate, thereby reducing experimental effort while maintaining predictive accuracy. Such approaches should be viewed as complementary to, rather than replacements for, the present physics-based framework, whose analytical transparency remains essential for interpreting the physical origin of the measured phase shift.

4.4. Limitations

A limitation of the present study is the use of a single excitation frequency (1 Hz) in the DMA measurements. While this choice ensures consistency with standard ASTM D4065-based testing protocols and allows direct comparison with existing literature on thermoplastic polymers and additively manufactured ABS, it does not capture the full frequency dependent viscoelastic response. Consequently, the proposed theoretical model is validated under a fixed-frequency condition, and its applicability across a broader frequency range is a subject of future studies.

In addition, the analysis is based on a single specimen geometry and a three-point bending configuration, which implies that the observed phase-shift behavior is inherently linked to the modal structure of the tested beam. Extension of the model to different geometries and loading configurations is therefore necessary to assess its generality. Moreover, the study focuses on a single material system (medical-grade ABS), and further work is required to evaluate whether the proposed modal interpretation of DMA phase shift remains valid for other thermoplastics and additively manufactured

polymers.

Furthermore, the quantitative fractographic void analysis presented here was limited to a single representative field of view of the FDM-printed specimen, owing to the limited field of view of the available optical micrographs. Future work employing scanning electron microscopy (SEM) or X-ray micro-computed tomography (μCT) would enable multi-section, three-dimensional quantification of void content and distribution across both sample groups, providing a more statistically robust basis for correlating porosity with mechanical performance.

4.5. Future work

Future work will directly address the limitations identified in the present study by extending the analysis to frequency-dependent DMA measurements, alternative specimen geometries, and additional polymer systems beyond medical-grade ABS. In particular, experimental investigations will be performed over a range of excitation frequencies to validate the proposed modal superposition framework beyond the single-frequency case considered here. Since the theoretical formulation given by Eq. (12) is valid for an arbitrary excitation frequency ω, the measured phase shifts obtained at different frequencies will be directly compared with the corresponding theoretical predictions. This comparison will enable assessment of the ability of the proposed modal framework to reproduce not only the temperature dependence of the phase shift, but also its frequency dependence over a broader dynamic range.

Future studies will also investigate alternative specimen geometries and loading configurations to further assess the generality of the proposed structure-dependent phase-shift formulation, as well as additional polymer systems beyond medical-grade ABS to clarify the extent to which the observed behavior is universal across additively manufactured thermoplastics. Finally, as discussed in the methodological outlook, data-driven and physics-informed approaches may provide a valuable complementary framework for surrogate modeling and optimization of thermo-mechanical responses in structured polymer systems.

5. CONCLUSIONS

The main contribution of this study is the demonstration that the DMA phase shift in beam-like polymer specimens should not be interpreted as a direct measure of a single intrinsic material relaxation process, but rather as an emergent structural quantity governed by the collective dynamics of multiple vibrational eigenmodes.

Beyond the specific case of medical-grade ABS, the present results demonstrate that the experimentally observed phase shift arises from a weighted superposition of multiple vibrational modes associated with the geometry of the tested specimen. This insight challenges the conventional lumped-parameter interpretation of DMA data and highlights the importance of structural dynamics in viscoelastic characterization.

The temperature-dependent viscoelastic behavior of medical-grade ABS was successfully captured using a combined experimental and theoretical approach. Dynamic mechanical analysis revealed that ABS samples produced by fused filament fabrication and injection molding exhibit nearly identical glass transition temperatures, indicating a comparable molecular structure of the polymer matrix. Nevertheless, 3D-printed specimens exhibit a reduced storage modulus over the investigated temperature range, attributed to printing-induced microstructural features, such as interlayer interfaces and local microvoids. Qualitative fractographic analysis supports this interpretation by revealing anisotropic crack propagation paths aligned with the filament deposition pattern.

Beyond experimental characterization, a theoretical model describing a damped vibrating beam was developed to interpret the DMA phase shift. Unlike the standard DMA formalism, the model demonstrates that each vibrational eigenmode possesses an individual phase shift, and that the experimentally measured phase lag corresponds to a weighted average over participating modes. By introducing a temperature-dependent effective damping coefficient, the model quantitatively reproduces the measured phase shift across the glass transition region. This agreement confirms that the observed temperature-dependent damping behavior can be consistently explained within a modal framework.

The results highlight the importance of structural dynamics in DMA measurements on beam-like polymer specimens, particularly those produced by additive manufacturing. The proposed approach provides a physically transparent link between macroscopic DMA observables and underlying vibrational mechanisms, offering a useful extension of conventional viscoelastic analysis for polymer structures with complex internal architecture.

Future studies will focus on extending the experimental validation to multiple excitation frequencies, alternative structural configurations, and additional polymer systems, thereby further assessing the generality of the proposed modal framework.

REFERENCES

1. Ventola CL. Medical applications for 3D printing: current and projected uses. Pharmacy and Therapeutics. 2014;39(10):704.
2. Gross BC, Erkal JL, Lockwood SY, Chen C, Spence DM. Evaluation of 3D printing and its potential impact on biotechnology and the chemical sciences. Analytical Chemistry. 2014;86(7):3240-53. Available from: https://doi.org/10.1021/ac403397r
3. Dong C, Petrovic M, Davies IJ. Applications of 3D printing in medicine: A review. Annals of 3D Printed Medicine. 2024;14:100149. Available from: https://doi.org/10.1016/j.stlm.2024.100149
4. Ali F, Kalva SN, Koc M. Advancements in 3D printing techniques for biomedical applications: a comprehensive review of materials consideration, post processing, applications, and challenges. Discover materials. 2024;4(1):53. Available from: https://doi.org/10.1007/s43939-024-00115-4
5. Mamo HB, Adamiak M, Kunwar A. 3D printed biomedical devices and their applications: A review on state-of-the-art technologies, existing challenges, and future perspectives. Journal of the Mechanical Behavior of Biomedical Materials. 2023;143:105930. Available from: https://doi.org/10.1016/j.jmbbm.2023.105930
6. Amaya-Rivas JL, Perero BS, Helguero CG, Hurel JL, Peralta JM, Flores FA, et al. Future trends of additive manufacturing in medical applications: An overview. Heliyon. 2024;10(5). Available from: https://doi.org/10.1016/j.heliyon.2024.e26641
7. Khan SB, Irfan S, Zhang Z, Yuan W. Redefining medical applications with safe and sustainable 3D printing. ACS Applied Bio Materials. 2025. Available from: https://doi.org/10.1021/acsabm.4c01923
8. Catasta A, Martini C, Mersanne A, Foresti R, Bianchini Massoni C, Freyrie A, et al. Systematic review on the use of 3D-printed models for planning, training and simulation in vascular surgery. Diagnostics. 2024;14(15):1658. Available from: https://doi.org/10.3390/ diagnostics14151658
9. Tasneem I, Ariz A, Bharti D, Haleem A, Javaid M, Bahl S. 3D printing technology and its significant applications in the context of healthcare education. Journal of Industrial Integration and Management. 2023;8(01):113-30.

Available from: https://doi.org/10.1142/ S2424862221500159
10. Paul GM, Rezaienia A, Wen P, Condoor S, Parkar N, King W, et al. Medical applications for 3D printing: recent developments. Missouri medicine. 2018;115(1):75.
11. Wang S, Chen X, Han X, Hong X, Li X, Zhang H, et al. A review of 3D printing technology in pharmaceutics: technology and applications, now and future. Pharmaceutics. 2023;15(2):416. Available from: https://doi.org/10.3390/pharmaceutics15020416
12. Gomase VS, Ghatule AP, Sharma R, Pathak S. Current 3D Printing Technologies and Their Potential Applications in Drug Delivery, Personalized Medicine & Pharmaceutical Sciences. Current Drug Discovery Technologies. 2025.
Available from:
https://doi.org/10.2174/0115701638392138250722112310
13. Tack P, Victor J, Gemmel P, Annemans L. 3D printing techniques in a medical setting: A systematic literature review. BioMedical Engineering OnLine. 2016;15(115).
Available from: https://doi.org/10.1186/s12938-016-0236-4
14. Wang C, Yang M, Chen L, et al. Polycaprolactone Strengthening Gelatin/Nano-Hydroxyapatite Composite Biomaterial Inks for Potential Application in Extrusion-Based 3D Printing Bone Scaffolds. Collagen & Leather. 2024;6:27. Available from: https://doi.org/10.1186/s42825-024-00170-w
15. Liu YY, Fernández Blázquez JP, Yin GZ, Wang DY, Llorca J, Echeverry-Rendón M. A strategy to tailor the mechanical and degradation properties of PCL-PEG-PCL based copolymers for biomedical application. European Polymer Journal 2023;198(17):112388. Available from: https://doi.org/10.1016/ j.eurpolymj.2023.112388
16. Pelin G, Pelin CE, Botan M, Cristea GC, Panait AAM. Thermo-mechanical properties of fused filament fabricated PLA at elevated temperatures. INCAS Bulletin. 2023;15(1):6.
Available from: https://doi.org/10.13111/2066-8201.2023.15.1.6
17. Kwon RY, Lew AJ, Jacobs CR. A microstructurally informed model for the mechanical response of three-dimensional actin networks. Preprint. 2008.
18. Chen Y, Huang J, et al. Tuning filament composition and microstructure of 3D-printed bioceramic scaffolds facilitate bone defect regeneration and repair. Regenerative Biomaterials. 2021;8(2):rbab007. Available from: https://doi.org/10.1093/ rb/rbab007
19. Nizam M, Purohit R, Taufik M. Materials for 3D printing in healthcare sector: A review. Proceedings of the Institution of Mechanical Engineers, Part H: Journal of Engineering in Medicine. 2024;238(10):939-63. Available from: https://doi.org/10.1177/ 09544119241289731
20. Ngo TD, Kashani A, Imbalzano G, Nguyen KTQ, Hui D. Additive manufacturing (3D printing): A review of materials, methods, applications and challenges. Composites Part B: Engineering. 2018;143:172-96. Available from: https://doi.org/10.1016/ j.compositesb.2018.02.012
21. Shilov SY, Rozhkova YA, Markova LN, Tashkinov MA, Vindokurov IV, Silberschmidt VV. Biocompatibility of 3D-Printed PLA, PEEK and PETG: Adhesion of bone marrow and peritoneal lavage cells. Polymers. 2022;14(19):3958.
Available from: https://doi.org/10.3390/polym14193958
22. Barchiki F, Fracaro L, Dominguez AC, Senegaglia AC, Vaz IM, Soares P et al. Biocompatibility of ABS and PLA polymers with dental pulp stem cells enhance their potential biomedical applications. Polymers. 2023;15(24):4629.
Available from: https://doi.org/10.3390/polym15244629
23. SGS Sp. z o.o. Filament Spectrum ABS Medical 1.75mm 1kg; 2025. Accessed: 2025-11-03. https://shop.spectrumfilaments.com/product-eng-1257-Filament-Spectrum-ABS-Medical-1-75mm-1kg.html.
24. Saldaña-Robles A, Sánchez-Angeles A, Balvantín-García AdJ, Núñez-Altamirano DA, Capilla-González G. Mechanical behavior of 3D printed polymers under tensile and bending loads. Advances in Science and Technology Research Journal. 2025;19(10):371-84. Available from: https://doi.org/10.12913/22998624/207989
25. Rendas P, Figueiredo L, Geraldo M, Vidal C, Soares B. Improvement of tensile and flexural properties of 3D printed PEEK through the increase of interfacial adhesion. Journal of Manufacturing Processes. 2023;93:260-74.
Available from: https://doi.org/10.1016/ j.jmapro.2023.03.024
26. Ahmad MN, Yahya A. Effects of 3D printing parameters on mechanical properties of ABS samples. Designs. 2023;7(6):136. Available from: https://doi.org/10.3390/designs7060136
27. Yahamed A, Ikonomov P, Fleming PD, Pekarovicova A, Gustafson P, Alden AQ, et al. Mechanical properties of 3D printed polymers. Journal of Print and Media Technology Research. 2016;5(4):273-89. Available from: https://doi.org/10.14622/JPMTR-1608
28. Struz J, Trochta M, Hruzik L, Pistacek D, Stawarz S, Kucharczyk W, et al. Wear and dynamic mechanical analysis (DMA) of samples produced via fused deposition modelling (FDM) 3D printing method. Polymers. 2024;16(21):3018.
Available from: https://doi.org/10.3390/polym16213018
29. Khan I, Kumar N, Choudhary M, Kumar S, Singh T. Mechanical and dynamic mechanical behavior of 3D printed waste slate particles filled acrylonitrile butadiene styrene composites. Arabian Journal of Chemistry. 2024;17(2):105559.
Available from: https://doi.org/10.1016/j.arabjc.2023.105559
30. Mohseni M, Hutmacher DW, Castro NJ. Independent Evaluation of Medical-Grade Bioresorbable Filaments for Fused Deposition Modelling/Fused Filament Fabrication of Tissue Engineered Constructs. Polymers. 2018;10(1):40.
Available from: https://doi.org/10.3390/polym10010040
31. Pitaru AA, Lacombe JG, Cooke ME, Beckman L, Steffen T, Weber MH, et al. Investigating Commercial Filaments for 3D Printing of Stiff and Elastic Constructs with Ligament-Like Mechanics. Micromachines. 2020;11(9):846. https://doi.org/10.3390/mi11090846
32. Szarlej P, Kucińska-Lipka J, Gubańska I, Janik H. Modifiers for Medical Grade Polymeric Systems used in FDM 3D Printing – Short Review. Biomedical Journal of Scientific & Technical Research. 2019;15(5):1–4. https://doi.org/10.26717/BJSTR.2019.15.002778
33. Zhai Y, Sun Z, Zhang T, Zhou C, Kong X. Mechanical Property of Thermoplastic Polyurethane Vascular Stents Fabricated by Fused Filament Fabrication. Micromachines. 2024;15(10):1266.
Available from: https://doi.org/10.3390/mi15101266
34. Trzaskowski M, Tanabe G, Churei H, Ueno T, Ziętala M, Wysocki B, et al. Physico-Mechanical Properties of 3D-Printed Filament Materials for Mouthguard Manufacturing. Polymers. 2025;17(16):2190. Available from: https://doi.org/10.3390/polym17162190
35. Skorski MR, Esenther JM, Ahmed Z, Miller AE, Hartings MR. The chemical, mechanical, and physical properties of 3D printed materials composed of TiO2-ABS nanocomposites. Science and Technology of advanced materials. 2016;17(1):89-97.
Available from: https://doi.org/10.1080/14686996.2016.1152879
36. Menard KP, Menard N. Dynamic mechanical analysis. CRC press; 2020.
37. Arunprasath K, Vijayakumar M, Ramarao M, Arul TG, Peniel Pauldoss S, Selwin M, et al. Dynamic mechanical analysis performance of pure 3D printed polylactic acid (PLA) and acrylonitrile butadiene styrene (ABS). Materials Today: Proceedings. 2022;50:1559–1562.
38. Kuzman MK, Ayrilmis N, Sernek M, Kariz M. Effect of selected printing settings on viscoelastic behaviour of 3D printed polymers with and without wood. Materials Research Express. 2019 Sep;6(10):105362. https://doi.org/10.1088/2053-1591/ab411c
39. Ghaznavi Youvalari A, Alizadeh Kaklar J, Mohamadi M. Investigation of mechanical properties in PLA, ABS and epoxy resin parts fabricated by 3D printing technology. Scientific Reports. 2025 Jul;15(1). https://doi.org/10.1038/s41598-025-13866-8
40. Dawoud M, Taha I, Ebeid SJ. Mechanical behaviour of ABS: An experimental study using FDM and injection moulding techniques. Journal of Manufacturing Processes. 2016 Jan;21:39–45. Available from: https://doi.org/10.1016/j.jmapro.2015.11.002
41. Boğa C. Investigation of mechanical and fracture behavior of pure and carbon fiber reinforced ABS samples processed by fused filament fabrication process. Rapid Prototyping Journal. 2021 Jun;27(6):1220–1229. Available from: https://doi.org/10.1108/RPJ-11-2020-0296

42. Lach R, Grellmann W, Han Y, Krüger P. In: Grellmann W, Seidler S, editors. Fracture Mechanics Characterization of ABS Materials — Influence of Morphology and Temperature. Berlin, Heidelberg: Springer Berlin Heidelberg; 2001; 317-34.
43. Czyżewski P, Marciniak D, Sykutera D. Mechanical properties of ABS samples manufactured under different process conditions. Bulletin of the Polish Academy of Sciences Technical Sciences. 2024;72:e147065.
Available from: https://doi.org/10.24425/bpasts.2023.147065
44. Tikhonov AN, Samarskii AA. Equations of mathematical physics. Mineola, NY: Courier Corporation; 2013.
45. Yamada K, Jl J. Substructure elimination method for evaluating bending vibration of beams. Mechanical Engineering Journal. 2023;10(6):23–00293–23–00293.
Available from: https://doi.org/10.1299/mej.23-00293
46. Zheng J, Hu H, Huang J, Zhao B, Huang H. CF-DeepONet: Deep operator neural networks for solving compressible flows. Aerospace Science and Technology. 2025 Aug;163:110329. Available from: https://doi.org/10.1016/j.ast.2025.110329
47. Zheng J, Li F, Huang H. T-phPINN: Physics-informed neural networks for solving 2D non-Fourier heat conduction equations. International Journal of Heat and Mass Transfer. 2024 Dec;235:126216. Available from: https://doi.org/10.1016/ j.ijheatmasstransfer.2024.126216
48. Zheng J, Huang J, Lin A, Li F, Huang H. Efficient surrogate-based optimization framework integrating physics-informed neural networks, deep active learning and deep reinforcement learning: Multilayer thin films case study. Engineering Applications of Artificial Intelligence. 2026 Feb;166:113609. Available from: https://doi.org/10.1016/j.engappai.2025.113609

Leszek Pyziak: https://orcid.org/0000-0003-4898-8911
Wiktoria Wojnarowska: https://orcid.org/0000-0001-7588-5294
Michał Wanic: https://orcid.org/0000-0002-4905-4988
Rafał Oliwa: https://orcid.org/0000-0003-1319-6199
Tomasz Więcek: https://orcid.org/0000-0002-4776-9357
Levan Chotorlishvili: https://orcid.org/0000-0001-7042-9273